IMMUNOLOGY

Vagus nerve stimulation modulates distinct acetylcholine receptors on B cells and limits the germinal center response

Izumi Kurata-Sato[1]†, Ibrahim T. Mughrabi[2]†, Minakshi Rana[1], Michael Gerber[2,3], Yousef Al-Abed[2], Barbara Sherry[4,5], Stavros Zanos[2,3,6], Betty Diamond[1,4]*

Acetylcholine is produced in the spleen in response to vagus nerve activation; however, the effects on antibody production have been largely unexplored. Here, we use a chronic vagus nerve stimulation (VNS) mouse model to study the effect of VNS on T-dependent B cell responses. We observed lower titers of high-affinity IgG and fewer antigen-specific germinal center (GC) B cells. GC B cells from chronic VNS mice exhibited altered mRNA and protein expression suggesting increased apoptosis and impaired plasma cell differentiation. Follicular dendritic cell (FDC) cluster dispersal and altered gene expression suggested poor function. The absence of acetylcholine-producing CD4$^+$ T cells diminished these alterations. In vitro studies revealed that α7 and α9 nicotinic acetylcholine receptors (nAChRs) directly regulated B cell production of TNF, a cytokine crucial to FDC clustering. α4 nAChR inhibited coligation of CD19 to the B cell receptor, presumably decreasing B cell survival. Thus, VNS-induced GC impairment can be attributed to distinct effects of nAChRs on B cells.

INTRODUCTION

Animal and clinical studies have demonstrated neural modulation of immunity (*1*–*4*). The mechanisms and pathways by which the nervous system controls immunity are intensively investigated (*5*, *6*), with the vagus nerve being the focus of many studies (*7*–*9*). Activation of the vagus nerve leads to activation of the splenic nerve which releases norepinephrine in the spleen. A specific subset of splenic CD4$^+$ T cells that expresses choline acetyltransferase (ChAT) responds to norepinephrine with the release of acetylcholine (ACh) (*10*). ACh produced by CD4$^+$ T cells exerts an immunosuppressive effect on splenic macrophages through engagement of α7 nicotinic acetylcholine receptors (nAChRs) (*6*). It is also known that several nicotinic and muscarinic ACh receptors are expressed on the surface of lymphocytes (*11*), but their immunomodulatory effects are less well studied.

The vagus nerve is activated in different inflammatory conditions, including sepsis (*12*, *13*). In the acute phase of sepsis, engagement of the vagus-immune pathway is beneficial as it suppresses potentially harmful inflammation to protect organ function (*14*). However, we have previously found that increased vagus nerve activation is sustained in postsepsis mice, leading to the diminished responsiveness of splenic macrophages to lipopolysaccharide (LPS) (*15*). We also reported an impaired germinal center (GC) response in postsepsis mice (*16*). Decreased tumor necrosis factor (TNF) production from antigen-activated B cells was associated with follicular dendritic cell (FDC) dispersion and lower titers of high-affinity antigen-specific antibody following immunization with a T-dependent (TD) antigen (*16*). Clinical studies also suggest insufficient humoral responses in sepsis survivors with poor vaccine responses and worse 5-year survival rates due to infections compared to those who do not experience sepsis (*17*, *18*). These observations led us to hypothesize that vagus nerve stimulation (VNS) alters the GC response.

The formation of the GC is a crucial process during the maturation of the antibody response. GCs are specialized microstructures formed in secondary lymphoid organs in response to antigen exposure. Following antigen activation, follicular (FO) B cells form GCs in cooperation with FDC clusters and T follicular helper (T_{FH}) cells (*19*). FDCs present antigens as immune complexes (*20*), while T_{FH} cells provide activation signals such as interleukin-21 and costimulatory molecules to GC B cells (*21*). In the GC, B cells undergo affinity-based selection (*22*) and differentiate into antibody-secreting plasma cells (PCs) and memory B cells. The modulation of the GC response by the vagus nerve has not been explored although B cells express α4β2 and α7 and α9 homomeric nAChRs (*11*, *23*–*26*). There are few in vivo studies about nAChR function on B cells: Zhang *et al.* (*24*) reported a contribution of α9 nAChR to PC expansion, while Fujii *et al.* (*27*) showed a potential effect of α7 nAChR on antibody production. An in vitro study indicates that these receptors influence different pathways within B cells (*23*), but our current understanding of neural mechanisms that regulate B cell function remains rudimentary. One of the reasons for the limited research on the in vivo effects on B cells is the difficulty of chronically manipulating vagus nerve activation.

Using a chronic VNS mouse model, we report that vagus nerve activation produces a reduced antibody response following immunization with a TD antigen. Mice subjected to chronic VNS produced a lower titer of high-affinity antibody. They also exhibited a lower number of antigen-specific GC B cells and decreased FDC clustering. The inhibitory effect of chronic VNS was diminished upon removal of ChAT$^+$ CD4$^+$ T cells. Moreover, we demonstrate, using in vitro studies, that ACh acts directly on B cells to reduce TNF production and B cell receptor (BCR) signaling, which are both critical for development of an effective GC response. Knockdown of the α7 and α9 nAChR subunits cancelled the reduction in TNF production, while knockdown of the α4 subunit restored BCR-induced Akt

[1]Center for Autoimmune Musculoskeletal and Hematopoietic Diseases, The Feinstein Institutes for Medical Research, Northwell Health, Manhasset, NY, USA. [2]Institute of Bioelectronic Medicine, The Feinstein Institutes for Medical Research, Northwell Health, Manhasset, NY, USA. [3]Donald and Barbara Zucker School of Medicine at Hofstra/Northwell, Manhasset, NY, USA. [4]Department of Molecular Medicine, Donald and Barbara Zucker School of Medicine at Hofstra/Northwell, Hempstead, NY, USA. [5]Center for Immunology and Inflammation, The Feinstein Institutes for Medical Research, Northwell Health, Manhasset, NY, USA. [6]Elmezzi Graduate School of Molecular Medicine, Manhasset, NY, USA.
*Corresponding author. Email: bdiamond@northwell.edu
†These authors contributed equally to this work.

phosphorylation. These distinct functions of the nAChR subtypes collaborate to inhibit a GC reaction. These results demonstrate one underlying mechanism for B cell hyporesponsiveness in conditions of increased vagus nerve activation and suggest a potential therapeutic approach to modulating the adaptive immune response.

RESULTS

Chronic VNS reduces antigen-specific GC B cells

To assess the effects of VNS on the humoral immune response, we implanted mice with cuff electrodes on the left cervical vagus nerve, through which they received 5 min of VNS twice daily while freely behaving in their cages (Fig. 1A). To assess longitudinal implant functionality and ensure successful engagement of the vagus nerve by stimulation, VNS-elicited reduction in heart rate was measured using implanted electrocardiogram (ECG) electrodes (fig. S1A). Mice received chronic VNS for 14 days before immunization with the TD antigen, 4-hydroxy-3-nitrophenylacetyl chicken γ-globulin (NP-CGG) in alum. VNS was continued for an additional 14 days to assess the effect on the antibody responses (Fig. 1B). Sham mice underwent surgery but were not implanted with VNS electrodes.

Serum from chronic VNS mice showed decreased high-affinity (anti-NP_2) immunoglobulin G (IgG) titers, whereas titers of low-affinity (anti-NP_{25}) IgG and IgM were comparable to those of sham mice after primary immunization (Fig. 1C). Total IgG was also comparable (fig. S1B). We enumerated NP-specific antibody-secreting cells in spleens by enzyme-linked immunospot (ELISpot) assay and found a reduction of anti-NP_2 IgG secreting cells in chronic VNS mice but no difference in anti-NP_{25} IgG secreting cells (Fig. 1D). Chronic VNS did not alter spleen weight, total B cell, nor total GC B cell frequencies (fig. S1, C to E; gating strategy shown in fig. S1E). Immunohistochemistry also showed comparable size of GC (Fig. 1F); however, chronic VNS decreased the frequency of NP-specific GC B cells (Fig. 1G). These data indicate that chronic VNS causes a diminished TD antigen–specific GC response with less high-affinity antibody production.

Chronic VNS impedes GC B cell maturation and survival

GCs are composed of a light zone (LZ) and a dark zone (DZ), each characterized by distinct cellular dynamics and interactions (*19*). The LZ, which contains FDCs, T_{FH} cells, and centrocytes, is where B cells undergo positive selection based on affinity for antigen. Centrocytes with weak antigen recognition undergo apoptosis, whereas positively selected centrocytes express CXCR4, become centroblasts, and move to DZ where they clonally expand (*28*). We sought to identify mechanisms underlying chronic VNS-induced GC impairment. We found an altered composition of GC B cells in chronic VNS mice with an increased percentage of centrocytes and a decreased percentage of centroblasts (Fig. 2A). Both GC subsets had higher expression of active caspase-3, an early apoptosis marker (Fig. 2B), suggesting diminished survival of GC B cells in chronic VNS mice. Furthermore, quantitative polymerase chain reaction (qPCR) of NP^+ GC B cells revealed increased *PAX5*, *BCL6*, and *BACH2* and decreased *PRDM1* (also known as Blimp1) mRNA expression in chronic VNS mice (Fig. 2C). PAX5 maintains a B cell state by repressing expression of PC genes like XBP1. BCL6 and BACH2 collaborate to repress the transcriptional program associated with PC differentiation, including the expression of PRDM1 (*29*, *30*). Diminished expression of Blimp1 was validated at protein level by flow cytometry (Fig. 2D). Immunohistochemistry showed increased expression of BCL6 in GC of chronic VNS mice (fig. S2A). To confirm these observations, we performed a single-cell transcriptome analysis of GC B cells (Fig. 2E). We identified five distinct GC B cell clusters among $B220^+$ $GL7^+$ NP^+ splenic cells [gating strategy is shown in fig. S2 (B to E)]. Centrocytes were identified on the basis of their relatively elevated expression levels of *Cd83* and *Cd86*, and centroblasts were identified by high expression of *Cxcr4* (fig. S2F). Chronic VNS did not alter gene expression profiles within the five clusters we identified (fig. S2G); however, we observed a reduction in the proportion of proliferating centroblasts with heightened expression of histone genes, *MKI67*, and *CDK1* (Fig. 2F). Gene expression profiles are shown in fig. S2 (H and I). We observed a cluster of centrocytes that trended higher in chronic VNS mice ($P = 0.1641$), characterized by elevated expression of *PAX5* and *BCL6* mRNA and less *XBP1* mRNA expression in comparison to the other centrocyte populations (fig. S2I), suggesting that these cells may be less exposed to differentiation signals provided by FDCs and T_{FH} cells (Fig. 2F). These findings indicate that GC B cells in chronic VNS mice exhibit a transcriptional program consistent with impaired survival and differentiation to PCs, which would contribute to the reduced NP-specific GC B cell response we observed.

Chronic VNS impairs FDC organization

FDC clusters in B cell follicles are the nidus for the GC response. They present antigens as immune complexes (*20*, *31*), and together with T_{FH} cells, they provide signals to B cells to promote somatic hypermutation and differentiation into PCs (*32*, *33*). Maintenance of FDC clusters is dependent on TNF, which is believed to be provided by B cells (*31*, *34*). In chronic VNS mice, gene expression analysis and flow cytometry revealed a reduction in TNF expression in GC B cells (Fig. 3, A and B), prompting us to examine FDC clusters. Although the relative abundance of FDCs identified as $CD35^+$ $CD45^-$ was not different between chronic VNS and sham mice (fig. S3, A and B), immunohistochemical analysis targeting CD35 demonstrated a decrease in the number and size of FDC clusters in the spleens of chronic VNS mice (Fig. 3, C to E), indicating a dispersal of FDCs. Tumor necrosis factor receptor 1 (*TNFR1*) and downstream IκB kinase (*IKK*β) mRNA expression were reduced in FDCs of chronic VNS mice (Fig. 3F). Diminished TNFR1 expression was validated with immunohistochemistry (Fig. 3G). TNFR1 is required for mature FDC function. It activates a canonical nuclear factor κB (NF-κB) pathway involving IKKβ/NF-κB essential modulator complexes (*34*, *35*) that is indispensable for GC B cell maturation (*35*). Previous papers have shown that expression of the complement receptor, CR2, is crucial for immune complex trapping (*35*, *36*). The mRNA expression level of *CR2* was also reduced in FDCs of chronic VNS mice compared to sham mice (Fig. 3F); intercellular adhesion molecule–1 (*ICAM-1*) and Fc γ receptor IIB (*FcγRIIB*) mRNA levels showed a trend toward decreased expression (Fig. 3F). Immunohistochemical evaluation of ICAM-1 showed a significant decrease in FDCs in the spleens of chronic VNS mice (Fig. 3H). These observations suggest diminished functionality in FDCs of chronic VNS mice.

$ChAT^+$ $CD4^+$ T cell mediates GC impairment

To address a potential cellular mediator of the altered B cell response in chronic VNS mice, we examined the impact on $ChAT^+$ $CD4^+$ T cells. ChAT reporter mice revealed an increase in $ChAT^+$ $CD4^+$ T cells in the spleen of chronic VNS mice (Fig. 4A). Approximately

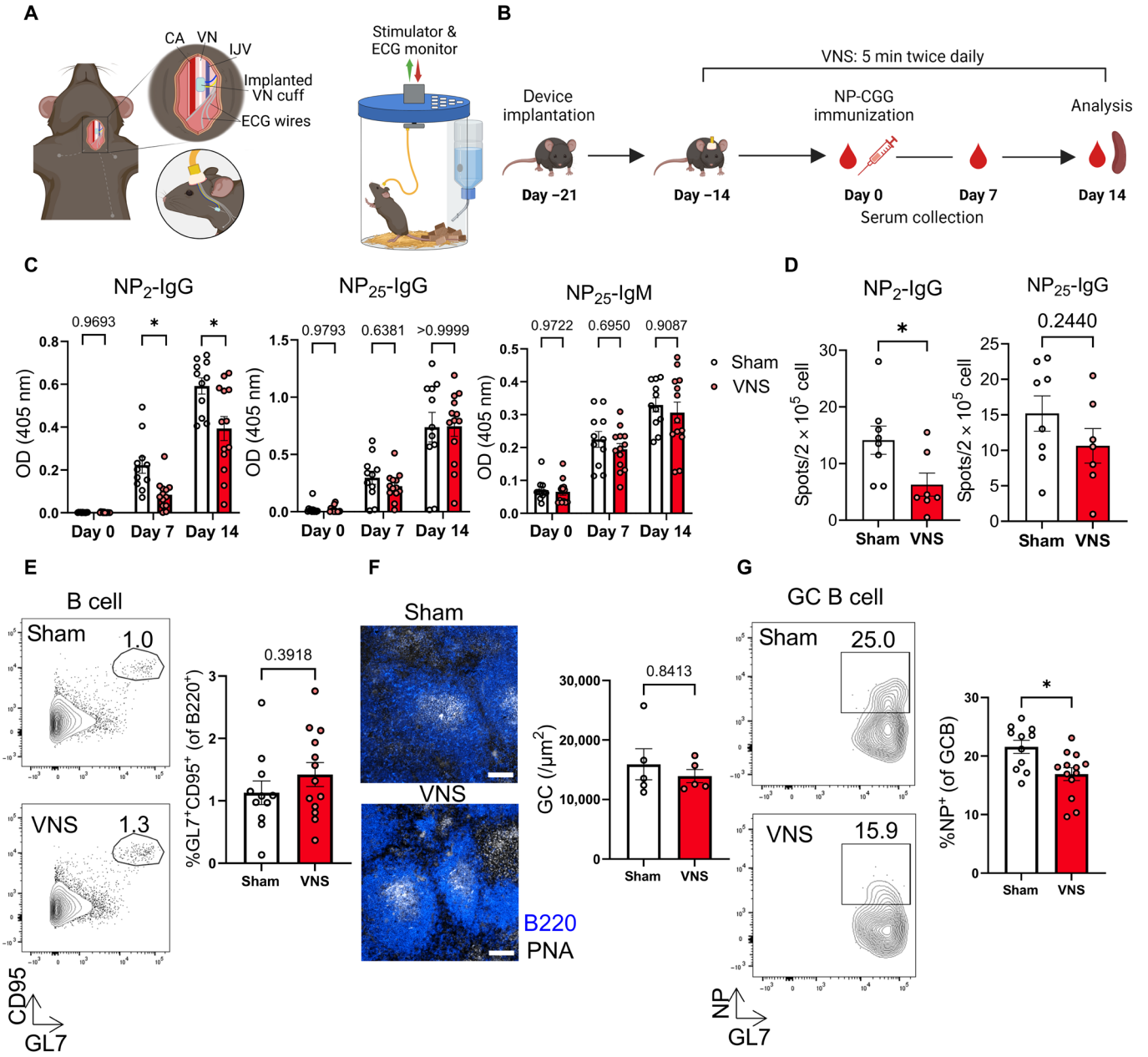

Fig. 1. Chronic VNS reduces the GC response. Mice implanted with a stimulation electrode on the left cervical vagus nerve received 5 min of VNS twice a day for 4 weeks while they were freely moving; a TD B cell response was assessed in these animals. (**A**) Schema of chronic vagus implant and home cage with integrated VNS system. (**B**) Experimental schema of chronic VNS. (**C**) Quantification of high-affinity (NP_2) and low-affinity (NP_{25}) anti-NP antibody titers in serum. (**D**) ELISpot assays of anti-NP antibody secreting cells on day 14 postimmunization. (**E**) Total GC B cells in spleen on day 14. Representative flow cytometry plots for each condition. (**F**) GC formation in spleen on day 14. Representative image of chronic VNS and sham spleens stained with anti-B220 (blue) antibody and peanut agglutinin (PNA; white). $B220^+$ PNA^+ spots were analyzed as GC. Scale bars, 100 μm. Five or six GCs were assessed with two different slides per mouse. Each dot represents an individual GC (top right) and individual mouse (bottom right). (**G**) NP-specific GC B cells in spleen on day 14. Representative flow cytometry plots for each condition. Data are shown as mean ± SEM with each symbol representing an individual mouse. Data are combined from two independent experiments. Asterisks indicate significant differences (*$P < 0.05$) obtained using two-way analysis of variance (ANOVA) (C) and Mann-Whitney *U* test [(D) to (G)]. CA, carotid artery; VN, vagus nerve; IJV, internal jugular vein. (A) and (B) Created with BioRender.com. OD, optical density.

30% of $ChAT^+$ $CD4^+$ cells had a T_{FH} phenotype ($CXCR5^+$ and $PD\text{-}1^+$), while only 5% of $ChAT^-$ $CD4^+$ cells were T_{FH}-like (fig. S4). We also studied mice lacking $ChAT^+$ T cells to address the impact of $ChAT^+$ T cells on the GC response. Chronic VNS mice lacking $ChAT^+$ $CD4^+$ T cells had more serum anti-NP_2 IgG and an increased frequency of NP-specific GC B cell compared to control ($CD4\text{-}cre\ ChAT^{wt}$) chronic VNS mice in response to NP-CGG immunization (Fig. 4, B to D). FDC clusters were enlarged in these mice although the number of clusters did not differ between mice with or without $ChAT^+$ T cells (Fig. 4, E to G). These data indicate that $ChAT^+$ $CD4^+$ T cells attenuate the GC response in chronic VNS mice.

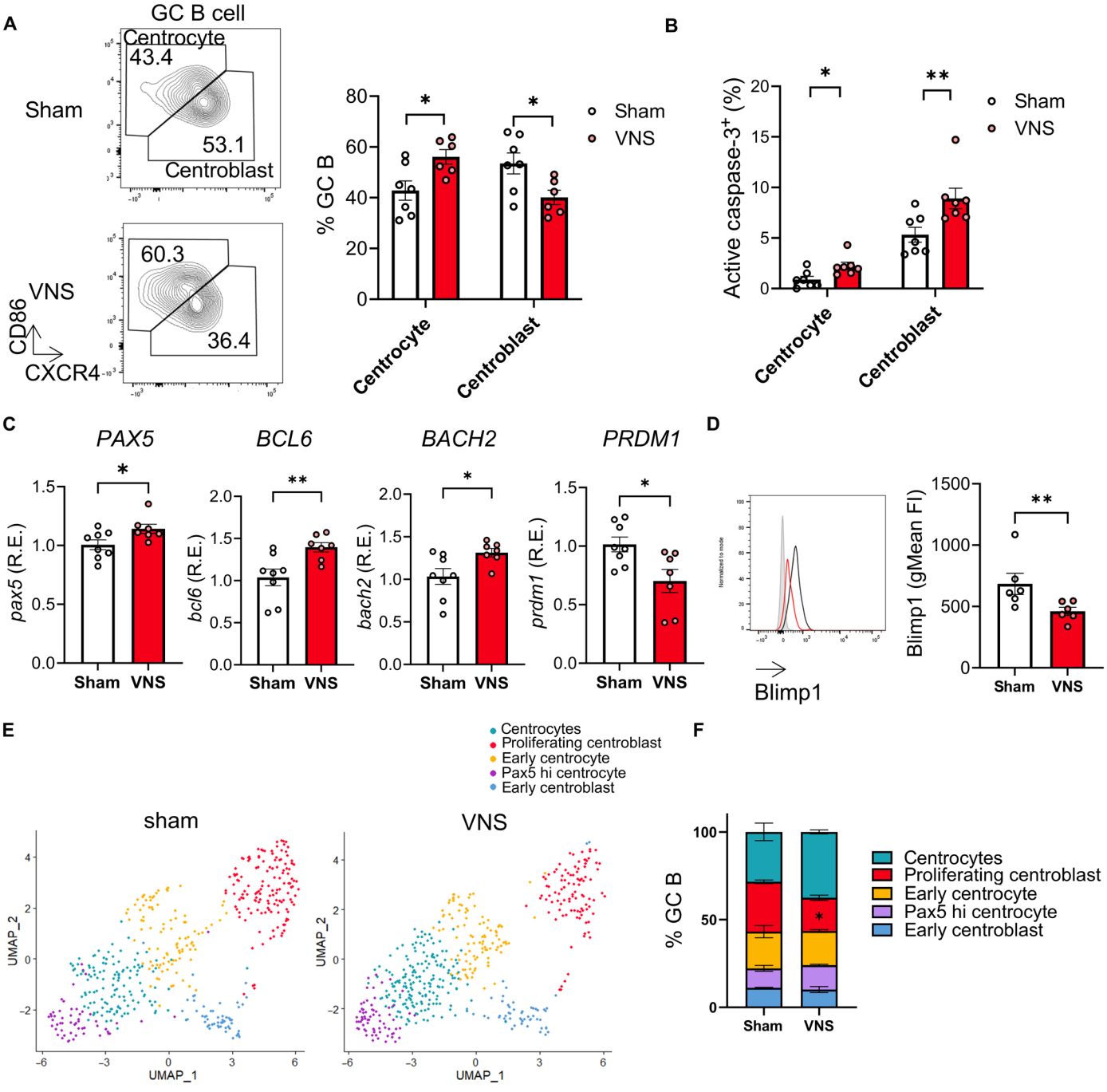

Fig. 2. Alteration of GC B cell composition and survival. Splenic B cells were collected from VNS and sham mice on day 14 and analyzed. (**A**) Centrocytes (LZ GC B cells) and centroblasts (DZ GC B cells) in VNS mice. (**B**) Frequency of active caspase-3$^+$ apoptotic cells in distinct GC B cell subsets assessed with flow cytometry. (**C**) Gene expression of sorted live NP$^+$ GC B cells was assessed with qRT-PCR. Relative expression to *Polr2a* is shown. (**D**) Blimp1 expression of NP-GC B cells was assessed with flow cytometry. Representative histograms for sham (black) and VNS (red) condition. Tinted gray histogram indicates a fluorescence-minus-one (FMO) control. Geometric mean fluorescent intensity was compared. (**E**) UMAP of GC B cell of sham and VNS mice. NP$^+$ GL7$^+$ B cells were sorted from four sham and four VNS mice and underwent single-cell analysis. After quality control, one sham and one VNS mouse were omitted from analysis because of the limited GC B cell numbers (<50). Each cluster was annotated using differentially expressed genes with the other clusters found by single-cell RNA sequencing (details shown in supplementary figures). (**F**) Proportion of each GC B cell cluster. Data are shown as mean ± SEM with each symbol representing an individual mouse from two [(A) to (D)] or single [(E) and (F)] independent experiments. Asterisks indicate significant differences (*P < 0.05 and **P < 0.01) obtained using Mann-Whitney U test. R.E, relative expression; FI, fluorescent intensity.

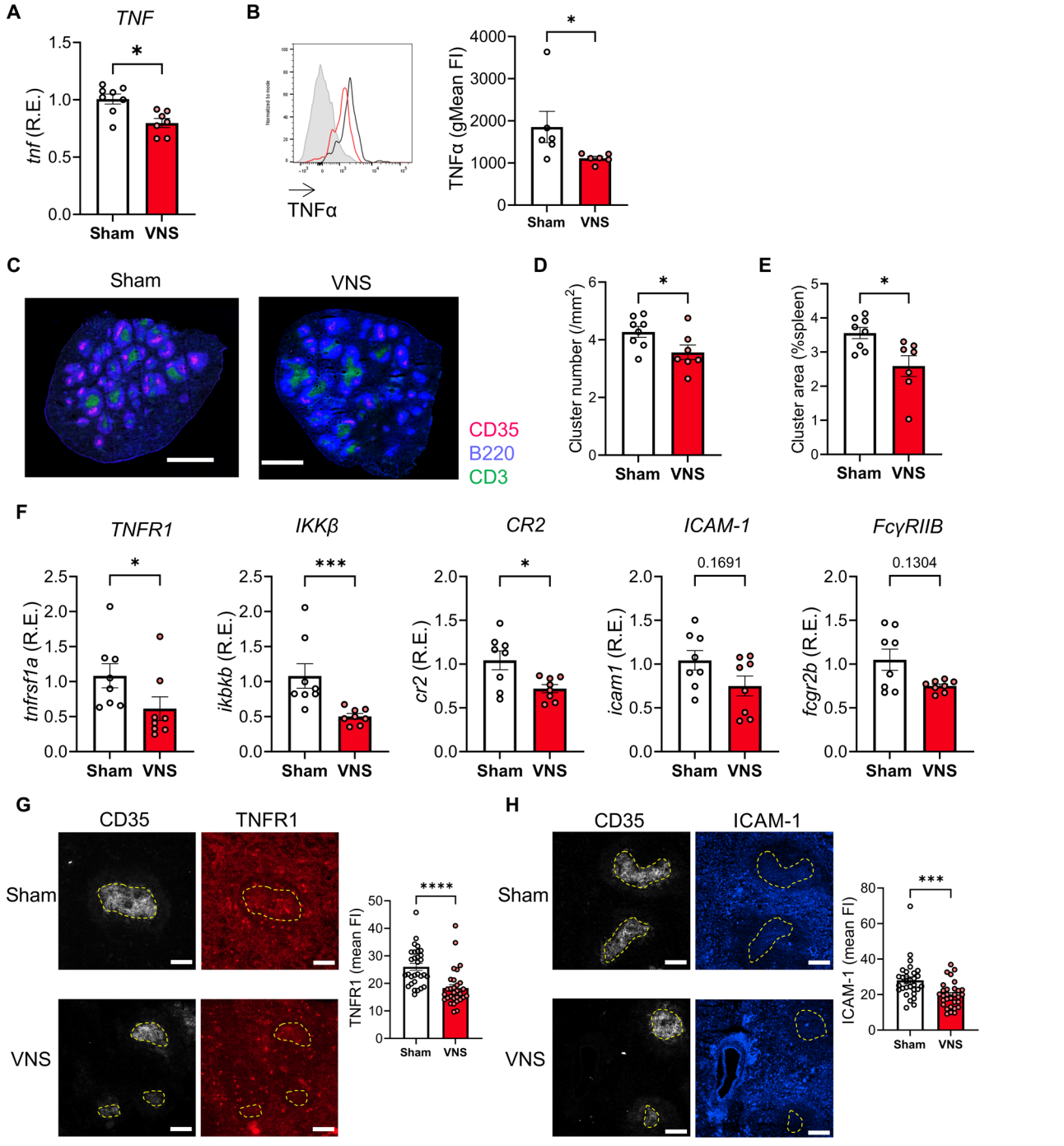

Fig. 3. Chronic VNS causes FDC dispersion, decreased TNF production by GC B cells, and altered FDC gene expression. Spleens were harvested from chronic VNS and sham mice at day 14 and analyzed. (**A**) TNF gene expression in total GC B cells sorted from the spleens at day 14. The expression was assessed by qRT-PCR. (**B**) TNFα expression of NP-GC B cells was assessed with flow cytometry. Representative histograms for sham (black) and chronic VNS (red) condition. Tinted gray histogram indicates FMO control. Geometric mean fluorescent intensity was compared. (**C**) Representative image of chronic VNS and sham spleens stained with anti-CD35 (magenta), anti-B220 (blue) and anti-CD3 (green) antibodies. Magenta spots were analyzed as FDC clusters. Scale bars, 1000 μm. FDC cluster numbers (**D**) and areas (**E**) were assessed. Two different slides per mouse were analyzed and averaged. Cluster numbers were counted manually. Areas were assessed with ImageJ software. Each dot represents an individual mouse. (**F**) Gene expression in FDCs sorted from chronic VNS and sham mice at day 14. Expression of the indicated genes was assessed by qRT-PCR. (**G**) TNFR1 and (**H**) ICAM-1 expression in FDC clusters on day 14. Representative image of chronic VNS and sham spleens stained with anti-CD35 (white), anti-TNFR1 (red), and anti–ICAM-1 (blue) antibodies. Fluorescence intensity of TNFR1 and ICAM-1 in $CD35^+$ lesion (yellow circle) was measured with ImageJ. Scale bars, 100 μm. Six clusters were assessed with two different slides per mouse. Five mice were assessed in each group. Each dot represents an individual cluster. Data are shown as mean ± SEM. Each symbol representing individual mouse combined from two independent cohorts. Asterisks indicate significant differences (*$P < 0.05$, ***$P < 0.001$, and ****$P < 0.0001$) obtained using Mann-Whitney *U* test.

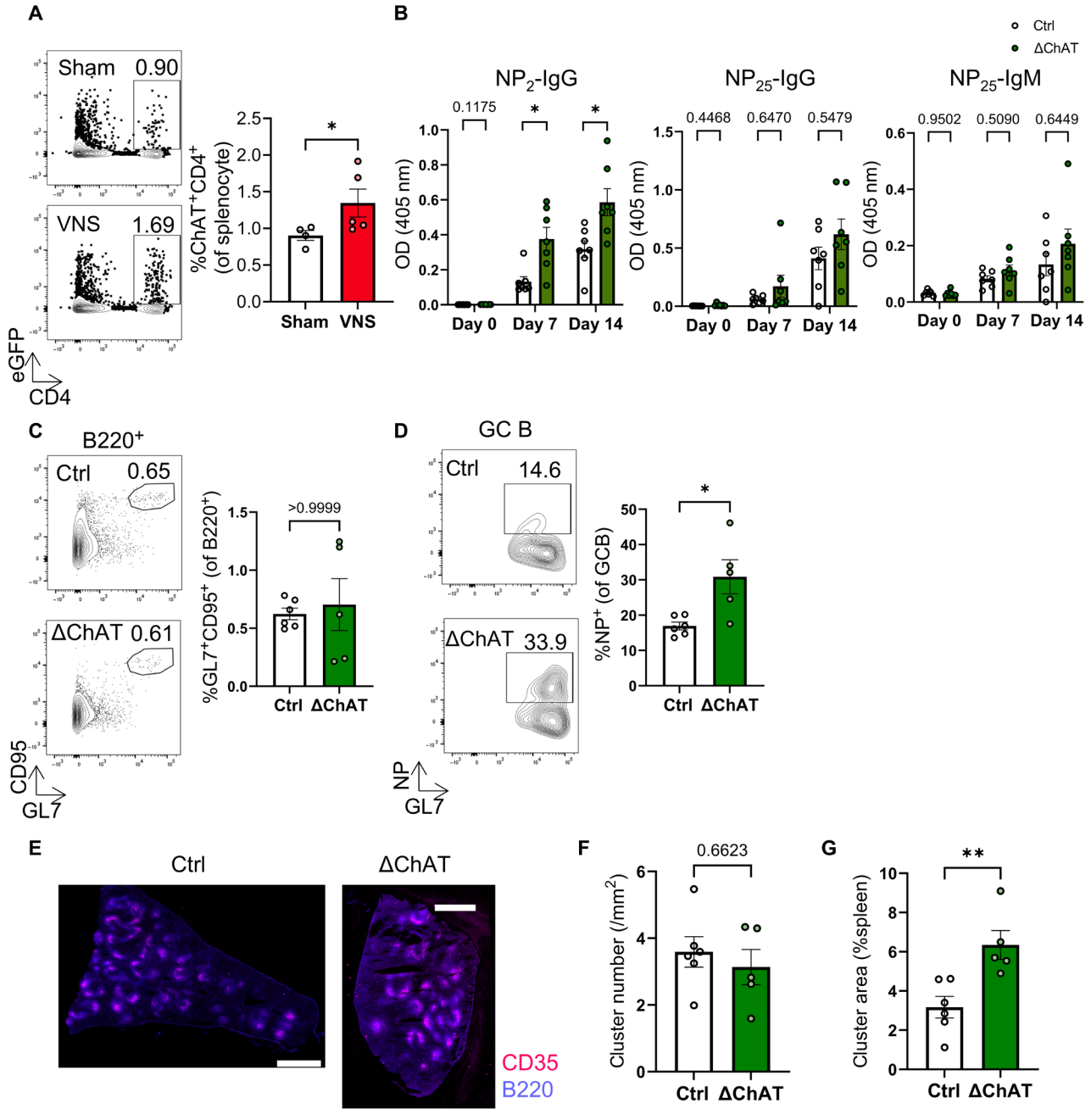

Fig. 4. CD4$^+$ ChAT$^+$ T cells impair the GC B cell response during chronic VNS. (**A**) Frequency of ChAT$^+$ T cells was analyzed using ChAT^{eGFP} reporter mice. Chronic VNS and sham mice were analyzed on day 14. (**B**) NP-specific antibody titers in serum from CD4-cre ChAT^{WT} (control) and CD4-cre ChAT $^{flox/flox}$ (ΔChAT) mice. Total (**C**) and NP-specific (**D**) GC B cells in spleens on day 14. (**E**) Representative images of splenic FDC clusters in control and ΔChAT mice. The numbers (**F**) and areas (**G**) were assessed using the same method as Fig. 3B. Data are shown as mean ± SEM with each symbol representing an individual mouse from one (A) or two [(B) to (D)] independent cohorts. Asterisks indicate significant differences (*P < 0.05, **P < 0.01) obtained using two-way ANOVA (B) or Mann-Whitney U test [(A), (C), (D), (F), and (G)].

AChR engagement directly impairs signaling pathways in B cells

Given that ChAT$^+$ CD4$^+$ T cells were implicated in the effects of chronic VNS on the GC response, we explored the direct impact of ACh on B cells. FO B cells stimulated in vitro with CpG, a Toll-like receptor 9 (TLR9) agonist, exhibited increased transcription of *TNF*. Coadministration of increasing doses of nicotine, a pan-nAChR agonist, decreased CpG-induced *TNF* mRNA in a dose-dependent fashion (Fig. 5A; the gating strategy of FO B cell is described in fig. S5A). This decrease was confirmed with a measurement of TNFα secreted into the culture supernatant (fig. S5B). Immunofluorescence showed decreased NF-κB p65 subunit translocation to the nucleus (Fig. 5B), a mechanism known to result in decreased TNF production (*37*).

We next examined phosphorylation of Akt downstream of BCR crosslinking (Fig. 5C), which is essential for antigen-mediated B cell survival (*38*, *39*). Akt phosphorylation was specifically inhibited by nicotine (Fig. 5D). As Akt activation requires proximity of the BCR with CD19 (*40*), we performed a proximity ligation assay and found that nicotine blocked the coligation of CD19 to the BCR (Fig. 5E) and subsequent CD19 phosphorylation (Fig. 5F) without altering CD19 and BCR expression (fig. S5, C and D). The expression of FcγRIIB and downstream SHIP1 activation, which are also known to regulate the PI3K-Akt pathway (*41*), were not altered (fig. S5, E and F). These data suggest that engagement of nAChR directly regulates TLR9 and BCR signaling pathways.

Different nAChR subtypes exhibit distinct patterns of localization and functionality

We hypothesized that nAChRs might physically interact with BCRs upon ACh engagement and prevent CD19 from entering the lipid raft where BCRs are located. Proximity ligation analysis showed that nAChRs with α4 subunits translocated toward the BCR in response to nicotine binding, whereas α7 subunits became more distant from the BCR and α9 subunits did not change their proximity (Fig. 6A).

To understand further the role of each nAChR, we performed small interfering RNA (siRNA)–mediated knockdown of specific nAChR subunits (fig. S6, A and B). The inhibition of TNF production was diminished in α7 and α9 nAChR-KD cells but not in α4 nAChR-KD cells (Fig. 6B). In contrast, inhibition of Akt phosphorylation was diminished only in α4 nAChR-KD cells (Fig. 6C). We additionally used B cells from B cell–specific α7 nAChR knockout (KO) mice to confirm that α7 nAChR is important for the inhibition of TNF production by nicotine; there was no effect of nicotine on Akt phosphorylation in B cells from α7 nAChR conditional KO mice (fig. S6, B and C). These data suggest that ACh directly alters B cell activation and function through distinct nAChR-mediated pathways.

DISCUSSION

In the present study, we studied the effects of chronic VNS on the B cell response to a TD antigen. We demonstrated that chronic VNS leads to a reduction in the high-affinity antibody response with fewer antigen-specific GC B cells. GC B cells in chronic VNS mice exhibited an increased propensity to undergo apoptosis and impaired differentiation into PCs. FDCs were dispersed and had an altered gene expression profile. In the presence of nicotine, B cells stimulated with CpG secreted less TNF and B cells stimulated through the BCR exhibited less phosphorylation of Akt. Knockdown experiments indicated that α7 and α9 nAChRs regulate TNF transcription via effects on NF-κB translocation, while α4β2 nAChR limits Akt phosphorylation by physically preventing the colocalization of the BCR and CD19. Together, our data indicate that the poor GC response in chronic VNS mice results from at least two distinct mechanisms: decreased TNF release from B cells triggering functional alterations in FDCs and impaired formation of the BCR-CD19 coreceptor complex leading to reduced Akt signaling and B cell survival.

Few studies have investigated neural modulation of humoral immune responses. Consistent with our findings, the α4β2 nAChR is reported to be located near the BCR (*23*). It is also important to note that TM4, a transmembrane domain of the nAChR, is thought to be a lipid sensor and influence the surrounding membrane lipid organization, particularly the lipid raft (*42*). It is plausible therefore to speculate that ACh may regulate the BCR complex through effects on lipid rafts after engagement of the BCR. The α7 nAChR stands out as one of the most extensively studied receptors in the realm of neural modulation of immunity. The global α7 nAChR KO mouse showed increased serum ovalbumin-specific IgG1 level (*27*), consistent with our findings. Also, the α7 nAChR has been documented to exert inhibitory effects on NF-κB translocation to the nucleus and TNF release from macrophages, especially in the context of endotoxemia (*7*, *14*). Whether α7 nAChRs on macrophages regulate an endosomal TLR pathway, as we observed in B cells, has not been investigated. It is also previously reported that α7 and α9 nAChRs are not involved in BCR-mediated activation (*23*). In contrast to these findings, Zhang *et al.* (*24*) reported that α9 nAChRs contribute to post-GC PC expansion. Their findings indicate that the splenic nerve promotes PC expansion through α9 nAChRs without affecting the GC B cell population. A distinction between their study and ours lies in our approach of applying chronic VNS 14 days before immunization, leading to FDC dispersion at the time of immunization, which was not observed in their study. Also, we adopted a regimen of twice-daily, 5-min VNS based on our previous finding that this regimen reduced serum TNF levels in response to LPS (*43*). Our regimen suppressed the GC response, but it is possible that distinct VNS parameters act differently on humoral immunity. In the present study, we found that different nAChRs play distinct roles. Given the varying binding affinities of these receptors (*44*), it is plausible that the outcome of ACh exposure differs based on the amount of ACh released.

The findings on FDC dispersion align with our previous findings in postsepsis mice in which the vagus nerve is constitutively activated (*15*, *16*), suggesting that the vagus nerve plays a role in impairing FDCs and thus dampening humoral immunity. However, it is essential to acknowledge that chronic VNS, as delivered in this study, did not fully replicate the postsepsis condition. Postsepsis mice displayed a more pronounced suppression in antibody production, affecting both high- and low-affinity antibodies (*16*). This may indicate the contribution of additional mechanisms or heightened vagus nerve activity.

It is also important to acknowledge that there could be other neurotransmitters and cell types at play during chronic VNS. Norepinephrine and dopamine are also reported to be increased by VNS (*45*), and immune cells including B cells have receptors for these molecules (*46*–*50*). As mice with ChAT-deficient $CD4^+$ T cells showed only a partial abrogation of the VNS effect, other pathways likely play a role in our model. Of interest, Suzuki *et al.* (*51*) showed β2 adrenergic receptors prevented T and B cell egress from lymph nodes through physical interactions with chemokine receptors. Furthermore, T_{FH} cells may be involved in VNS-mediated changes in the GC response because $CD4^+$ T cells also express both nAChRs and adrenergic receptors (*11*). We found an increase of CXCR5 expression of $ChAT^+$ $CD4^+$ T cells in chronic VNS mice (fig. S4A), suggesting that chronic VNS may affect migration of these cells within the spleen, ultimately contributing to modulation of the GC response.

In this study, mice without cuff implantation were used as sham controls. This decision was based on our prior observation that the presence of the cuff itself did not elicit any discernible impact on the acute TNF response to LPS (*43*). In addition, previous studies that used chronic VNS in rats, where control animals were implanted with a vagus nerve cuff, showed no anti-inflammatory effect in the sham-stimulated group including no effect on TNF levels in target tissues (*52*). Further, a study in mice showed that acute hooking or

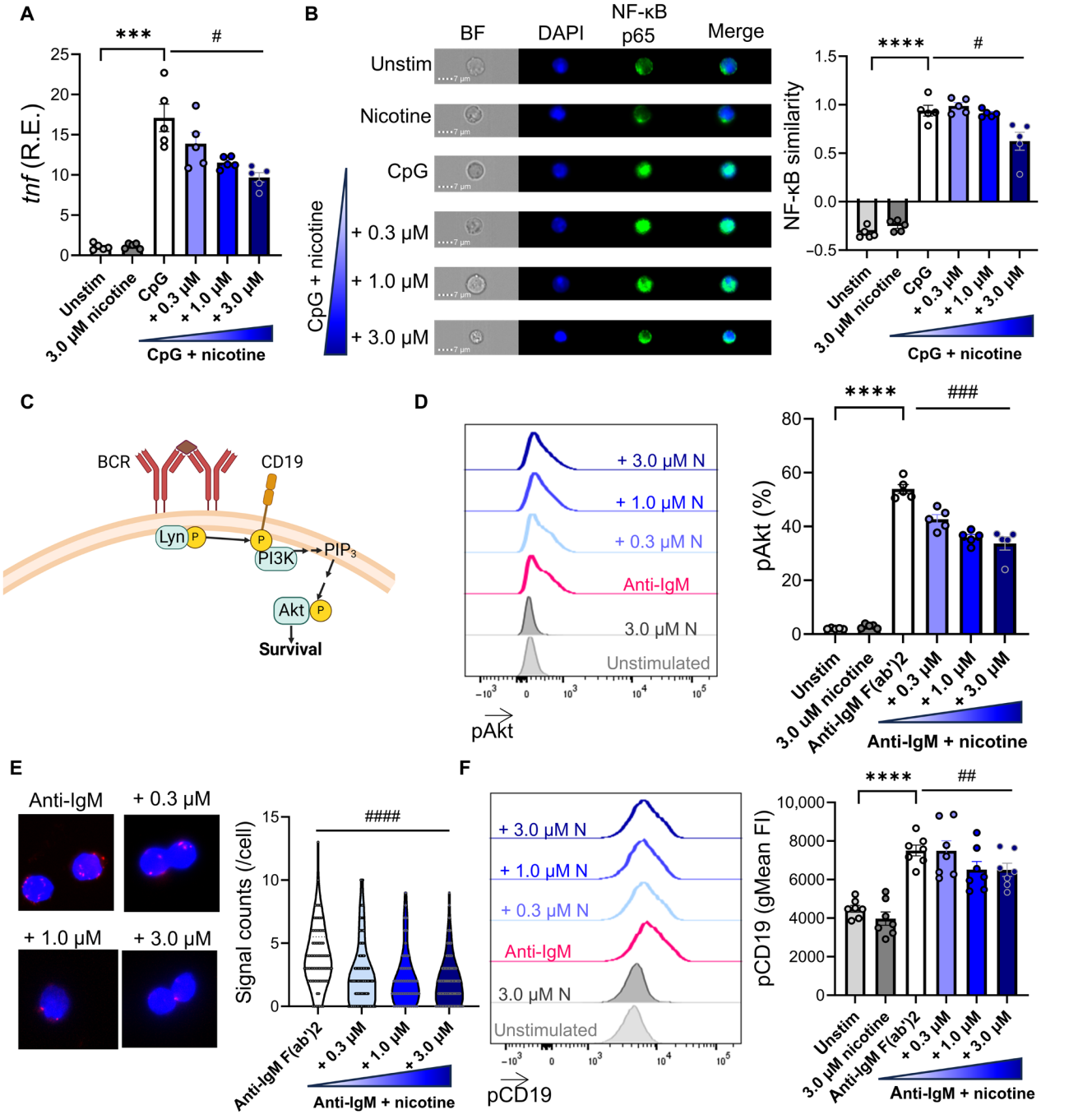

Fig. 5. ACh directly regulates TLR9 signaling and BCR-mediated Akt phosphorylation via nicotinic receptors. (**A**) TNF mRNA in nicotine exposed, CpG-treated FO B cells. Splenic FO B cells from untreated mice were sorted using flow cytometry and incubated with 2.5 μM CpG and/or the indicated amount of nicotine. Cells were collected after 4 hours incubation, and qRT-PCR was performed. (**B**) NF-κB p65 translocation to nucleus following CpG stimulation with or without nicotine exposure. Total B cells were isolated from untreated mice using magnetic sorting. Cells were incubated with the indicated amount of nicotine and/or 1.0 μM CpG for an hour. NF-κB p65 translocation was assessed by comparing similarity of 4′,6-diamidino-2-phenylindole (DAPI) and NF-κB staining morphology using imaging cytometry. (**C**) Scheme of BCR signaling pathways. Created with BioRender.com. (**D**) Phosphorylation of Akt (S473) following BCR activation with or without nicotine exposure. Splenocytes were collected from untreated mice and stimulated with or without nicotine and anti-IgM F(ab′)2. Phosphorylated Akt in FO B cells was quantified using flow cytometry. (**E**) Proximity ligation assay with membrane IgM and CD19. Total B cells were isolated from untreated mice and incubated with anti-IgM F(ab′)2 with or without nicotine. Proximity of membrane IgM and CD19 was assessed by counting signal spots. Three mice were assessed per condition, and three independent fields were analyzed per sample. (**F**) Phosphorylation of CD19 following BCR activation and nicotine exposure assessed using the same method as (D). Each dot represents an individual mouse. Data are shown as mean ± SEM [(A), (B), (D), and (F)]. Data from two to three independent experiments were combined and assessed. Hash marks indicate significant differences (#$P < 0.05$, ##$P < 0.01$, ###$P < 0.001$, and ####$P < 0.0001$) obtained using one-way repeated measure ANOVA test with Geisser-Greenhouse correction. Asterisks indicate significant differences (***$P < 0.001$, and ****$P < 0.0001$) obtained using paired *t* test. BF, bright field; N, nicotine.

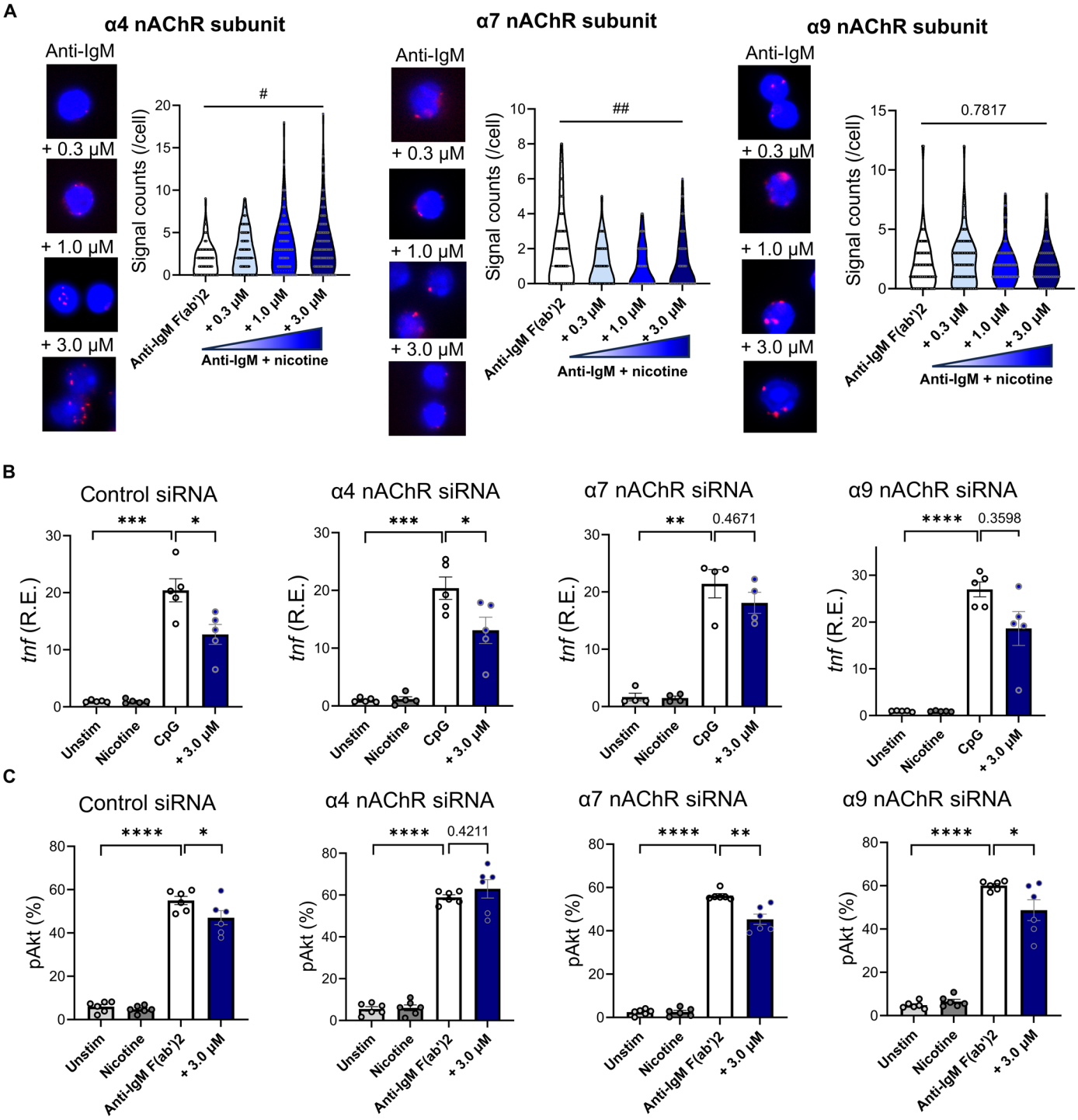

Fig. 6. α7 and α9 nAChRs regulate TNF production and α4 nAChR regulate BCR signaling. (**A**) Proximity ligation assay with membrane IgM and nicotinic ACh receptor subunits, assessed with the same method as Fig. 5F. Three mice were assessed per condition, and three independent fields were analyzed per sample. (**B**) TNF mRNA in nAChR knocked down B cells. B cells were transfected with siRNA for each nAChR subunit or control. Transfected cells were isolated by flow cytometry and subsequently stimulated with CpG and nicotine. (**C**) Akt (S473) phosphorylation of nAChR knocked down FO B cells. B cells were transfected with siRNA for each nAChR or control siRNA. Transfected cells were isolated by flow cytometry and subsequently incubated with anti-IgM F(ab′)2 and nicotine. FO B cells were identified by flow cytometry (gating strategy is shown in fig. S5A). Data are shown as mean ± SEM [(B) and (C)]. Data from two to three independent experiments were combined and assessed. Hash marks indicate significant differences (#$P < 0.05$, ##$P < 0.01$) obtained using one-way repeated measure ANOVA test with Geisser-Greenhouse correction. Asterisks indicate significant differences (*$P < 0.05$, **$P < 0.01$, ***$P < 0.001$, and ****$P < 0.0001$) obtained using paired *t* test.

mechanical manipulation of the vagus nerve did not lead to suppression of TNF after an LPS challenge (*53*).

It is worth noting that stimulation of the cervical vagus nerve, where all afferent and efferent vagal fibers converge, engages several autonomic circuits and reflexes (*6*) whose activation was not evaluated in this study. Some of these pathways, including preganglionic, sympathetic fibers in the splanchnic nerve that project to the celiac ganglion (*6*), may be involved in the effects of chronic VNS that we report. Their contribution will have to be determined in future studies.

In summary, we have revealed pathways through which the vagus nerve regulates humoral immunity. These findings have potential clinical significance in reversing undesired immunosuppression or in diminishing an exuberant GC-derived autoantibody response (*17*, *18*, *54*). Altering vagus nerve activity could be a new therapeutic strategy to reverse this immunosuppressed state which may be present also in survivors of severe COVID-19 infection.

MATERIALS AND METHODS

Mice and immunization

Male C57BL/6 were purchased from the Jackson Laboratory and Charles River Laboratories and used at 8 to 15 weeks of age. ChAT^{eGFP} mice on a CD57BL/6 background were a gift from K. Tracey. CD4-cre, ChAT^{flox}, CD19-cre, and CHRNA7^{flox} mice, all on a CD57BL/6 background, were purchased from the Jackson Laboratory and bred at the Feinstein Institutes for Medical Research for more than 10 generations (detailed information of strains is found in table S1). All mice were housed under specific pathogen–free conditions. In some experiments, mice were administered 100 μg of NP-CGG (Biosearch Technologies) emulsified in 100 μl of Imject alum (Thermo Fisher Scientific) by intraperitoneal injection. Mice were euthanized by CO_2 overdose or by cervical dislocation at the time points indicated in Results. Serum was obtained by tail bleeding or by cardiac puncture. All protocols including VNS were approved by the Institutional Animal Care and Use Committee.

Vagus nerve and ECG electrodes implantation

Commercial micro-cuff electrodes (100-μm microsling, CorTec, Germany) and platinum iridium wires were integrated onto a nano-strip connector (Omnetics). The cuff electrodes were implanted on the left cervical vagus nerve, and the platinum iridium wires were tethered subcutaneously to the chest wall to record ECG as described previously (*43*). Briefly, anesthesia was induced with 3 to 4% isoflurane and maintained with 1.5%. On a warmed surgical pad, an area over the dorsal skull was exposed and scrubbed with saline and hydrogen peroxide, and a subcutaneous tunnel to the ventral neck was created. The carotid sheath was exposed through a ventral neck incision, and the left vagus nerve was gently dissected away from the sheath. The cuff and ECG electrodes were tunneled to the ventral neck through the skull incision, and the cuff electrode was carefully placed on the vagus nerve and embedded under neck musculature. The ECG electrodes were sutured subcutaneously to the upper and lower chest wall through the ventral neck and a left subcostal incision. The strip connector was then cemented to the skull and sealed with surgical glue. The surgery was performed under strict aseptic technique. Mice were supplemented with saline throughout the procedure and treated with meloxicam (5 mg/kg) postoperatively. Mice were allowed to recover for about a week before starting chronic VNS.

Chronic VNS

Mice were singly housed in custom-made cages (Fig. 1A) each comprising a clear acrylic cylinder (15.24 cm in diameter, 20.32 cm in height), a three-dimensional–printed ventilated plastic cover with an integrated commutator system (P1 Technologies), and a water bottle. Food and nestlet material were provided on the floor of the cage and were changed weekly. Mice were acclimated to these cages for 1 week before receiving the implant surgery and continued to be housed in their home cages till the end of the experiment. After 1 week of recovery, mice were connected to the commutator via a flexible cable which allows free movement. The commutator system was connected to a battery-operated stimulating/recording system [Neurochip 3 (*55*)] located outside the cage and programmed with stimulation parameters and schedule. The custom-made cages were placed on a mobile station and housed in the mouse vivarium on a 12-hour light/dark cycle with ad libitum access to food and water. Mice received twice-daily stimulation (6 hours apart) using the following parameters: 500-μs pulse width, 30-Hz frequency, and 5-min duration at a current intensity that caused ~20 to 30% reduction in baseline heart rate. The recorded ECG was reviewed daily to monitor the functionality of the stimulating electrode and adjust stimulation intensity to maintain a consistent heart rate response throughout the period of VNS. Mice were monitored daily to observe indicators of wellbeing, including food and water consumption and nest building. On weeks 2 and 3 of VNS (Fig. 1B), blood was collected by tail-tip sampling under isoflurane anesthesia for serological assays. At the end of week 4 of VNS, mice were euthanized, and spleen and blood were collected for analysis.

Enzyme-linked immunosorbent assay

Serum titers of NP-specific antibodies, total IgG, and IgM were measured by enzyme-linked immunosorbent assay. Half-area flat-bottom plates were coated with NP_2 or NP_{25}–bovine serum albumin (BSA) (10 μg/ml; Biosearch Technologies) or goat anti-mouse IgG (5 μg/ml; Southern Biotech) overnight at 4°C. Plates were then washed six times with 0.05% Tween/phosphate-buffered saline (PBS) solution and blocked with 1% BSA/PBS at room temperature for an hour. Serum diluted with 0.2% BSA/PBS (1:2000 for anti-NP IgG, 1:20,000 for total IgG) was added to the wells. After 2 hours of incubation, plates were washed, and alkaline phosphatase (AP)–conjugated goat polyclonal anti-mouse IgG (Southern Biotech) diluted with 0.2% BSA/PBS (1:1000) was added and incubated for an hour, followed by color development with phosphatase substrate (1 mg/ml; Millipore Sigma). The color absorbance of each well was read at 405 nm on 1430 Multilabel Counter Spectrometer (PerkinElmer).

ELISpot

For counting NP-specific antibody producing cells, 96-well Immulon 4HBX plates (Thermo Fisher Scientific) were coated with of NP_2- or NP_{25}-BSA (10 μg/ml) in PBS overnight at 4°C. Plates were washed and blocked with RPMI 1640 (Gibco) supplemented with 10% heat-inactivated fetal bovine serum (FBS), 1% penicillin/streptomycin, and 10 mM Hepes for an hour at 37°C to avoid nonspecific binding. Serially diluted splenocytes suspended in the supplemented RPMI 1640 were added to the wells. Plates were incubated overnight at 37°C and washed in the following day. Wells were incubated with biotinylated goat anti-mouse IgG/IgM (Southern Biotech) for 2 hours

at 37°C, followed by AP-conjugated streptavidin (Southern Biotech) for an hour at 37°C. Spot development was performed using the Vector Blue Alkaline Phosphatase Substrate Kit (Vector Laboratories) according to the manufacturer's instruction. Spots were counted manually.

Flow cytometry and cell sorting

A single-cell suspension of spleens was obtained by mechanical dissociation. Cells were suspended in flow cytometry buffer (2% FBS, 0.1% NaN_3, and 1 mM EDTA in Hanks' balanced salt solution) at 1×10^7 cells/ml and incubated with Fc block (anti-mouse CD16/32; clone 93, BioLegend) for 10 min before incubation with specific antibodies listed in table S1, except for FcγRIIB staining. Dead cells were stained out with Fixable Viability Dye (Thermo Fisher Scientific). For detection of NP-specific B cells, biotinylated NP-BSA (Biosearch Technologies) was incubated with allophycocyanin (APC)-conjugated streptavidin (BioLegend) before being added to the cell suspension. For active caspase-3 staining, Cytofix/Cytoperm buffer (BD Biosciences) was used according to the manufacturer's instructions. For Blimp1 and TNFα staining, Foxp3/Transcription Factor Staining Buffer (Invitrogen) was used according to the manufacturer's instructions. Cells were analyzed with a BD LSR Fortessa X-20 flow cytometer (BD Biosciences) and FlowJo software v10.7.2 (Tree Star) or sorted with a fluorescence-activated cell sorting Aria (BD Biosciences). Sorting purity of FDCs was confirmed by flow cytometry (>80%). Sorted cells then underwent stimulation or were stored in TRIzol reagent (Life Technologies) at −80°C for mRNA extraction. Some experiments were performed with frozen cells.

Quantitative real-time PCR

mRNA was extracted from cells using a Direct-zol RNA Microprep kit (Zymo Research) according to the manufacturer's instructions. Freshly isolated mRNA was reverse-transcribed into cDNA with random primers by the iScript cDNA Synthesis Kit (Bio-Rad).

Quantitative reverse transcription PCR (RT-PCR) was performed on LightCycler 480 II (Roche) using TaqMan gene expression assay (Thermo Fisher Scientific). Primers used for assays are listed in table S1. Relative gene expression was normalized to expression of RNA polymerase II subunit A (polr2a) using the $2^{-\Delta\Delta Ct}$ method. For GC B cell and FDC gene expression, synthesized cDNA was subjected to preamplification of target genes as well as polr2a using the TaqMan PreAmp Master Mix Kit (Thermo Fisher Scientific) before qRT-PCR.

Single-cell RNA sequencing

$B220^+$ $GL7^+$ NP^+ cells were sorted from chronic VNS ($n = 4$) and sham ($n = 4$) mice at day 14 by flow cytometry. The gating strategy is described in fig. S2A. Each sample was tagged with different TotalSeq-C hashing antibody (BioLegend). Library preparation was performed according to the manufacturer's instructions (Next GEM Single Cell 5′GEM v3.1 protocol, 10x Genomics). Libraries were sequenced by MedGenome on an Illumina NovaSeq. FASTQ data from 10x Chromium were processed with CellRanger v6.1.238 aligning to the C57BL/6 reference genome. The count matrix was loaded into R and further processed using the Seurat R package v4.9.9, EnhancedVolcano, and DESeq2. Doublets and empty droplets were determined and excluded by analyzing hashing oligos. Cells with fewer than 200 distinct genes or with more than 5% of mitochondrial genes were also excluded as low-quality cells. The remaining cells were clustered using Uniform Manifold Approximation and Projection (UMAP) (resolution = 0.8). Four clusters which highly expressed *Cd3e* or *Itgam* and did not express *Ms4a1* were annotated as contamination of T and myeloid cells and subsequently excluded. Four clusters (3, 4, 6, 7) were determined as the GC B cell clusters using known markers (*Aicda*, *S1pr2*, *Fas*, and *Bcl6*; fig. S2C). One chronic VNS and one sham mice were omitted due to relatively small number of GC B cells (<50 cells). These clusters were extracted and reanalyzed for differential gene expressions (fig. S2D) and frequencies.

Immunofluorescence

Freshly isolated spleens were half-cut, embedded in optimal cutting temperature compound (Thermo Fisher Scientific), frozen at −80°C, and cut at 8-μm thickness with a cryostat. For FDC staining, sections were fixed with cold acetone for 10 min. Sections were then blocked in PBS with 8% normal rat serum for 1 hour before staining. Slides were stained with biotinylated anti-mouse CD35 (diluted in 1:100), APC-conjugated anti-mouse CD3 (1:100), Brilliant Violet 421–conjugated anti-mouse B220 (1:200), anti-mouse CD120α (TNFR1), and/or anti-mouse ICAM-1 in 2% normal rat serum/PBS overnight at 4°C. Slides were subsequently washed and incubated with Alexa Flour 568–conjugated streptavidin, Alexa Flour 647–conjugated goat anti-Armenian hamster IgG, and/or Brilliant Violet 421–conjugated donkey anti-rabbit IgG for 45 min at room temperature.

For GC staining, sections were fixed with 10% formalin for 10 min and permeabilized with 0.2% Triton X-100/PBS for 30 min. Sections were then blocked in 2% BSA and 5% normal goat serum/PBS for 1 hour at room temperature. Slides were incubated with Brilliant Violet 421–conjugated anti-mouse B220 antibody (1:200), Cy3-conjugated peanut agglutinin (1:200), anti-mouse BCL6 antibody (1:100) in 2% BSA, 5% normal goat serum/PBS for overnight at 4°C, followed by Alexa Fluor 647–conjugated anti-rabbit antibody.

All slides were mounted with Dako Fluorescence Mounting Medium (Dako) and analyzed with a Zeiss Apotome 3 microscope (Zeiss). Imaging data were analyzed with ImageJ. Two independent slides were assessed per spleen. Antibodies used are listed in table S1.

For imaging cytometry, stimulated cells were fixed and permeabilized overnight with Foxp3/Transcription Factor Staining Buffer Set. Anti–NF-κB p65 antibody (diluted in 1:500) was added and incubated for an hour, followed by AF488-conjugated anti-rabbit IgG. After washing, cells were stained with 4′,6-diamidino-2-phenylindole (DAPI). NF-κB translocation was assessed with Amnis ImageStreamX Mk II (Luminex). For each condition, 400 cells per mouse were collected and analyzed. The similarity score was obtained from IDEAS software, which calculated fluorochrome distribution similarity between anti-NF-κB antibody and DAPI. Antibodies used are listed in table S1.

In vitro cell stimulation

For measurements of TNF mRNA, FO B cells were sorted (the gating strategy is shown in fig. S4A) and stimulated with 2.5 μM CpG (InvivoGen) and nicotine (Sigma-Aldrich) in RPMI 1640 (Gibco) supplemented with 10% heat-inactivated FBS, 1% penicillin/streptomycin and 10 mM Hepes. After 4 hours of incubation, cells were collected, and pellets were solubilized in TRIzol reagent. These solution were stored at −80°C. For measurement of secreted TNFα, the culture supernatant was collected after 24 hours of incubation. TNFα concentration was measured with the V-PLEX Mouse TNF-α Kit (Meso Scale Diagnostics) and the Sector Imager 2400 Reader (Meso Scale Diagnostics) according to the manufacturer's instructions.

For NF-κB translocation assays, B cells were isolated from naïve mouse spleens with the EasySep Mouse Pan-B cell Isolation Kit (STEMCELL Technologies) and suspended at 1.0×10^6 cells/ml in the supplemented RPMI 1640 (Gibco). Cells were stimulated with 1.0 μM CpG with or without nicotine for an hour. After washing, cells were fixed and permeabilized using Foxp3/Transcription Factor Staining Buffer.

BCR signal analysis

Single-cell suspensions were obtained from untreated mouse spleens and rested in the supplemented RPMI 1640 at 37°C for an hour before stimulation. Cells were then stimulated with nicotine for 20 min and subsequently anti-mouse IgM F(ab′)2 (Jackson ImmunoResearch) for 2 min (pCD19) or 5 min (pAkt). Stimulation was ceased by adding prewarmed Lyse/Fix buffer (BD Biosciences). Fixed cells were then incubated with Perm/Wash buffer (BD Biosciences) for 30 to 60 min and stained with antibodies listed in table S1.

Western blot

Western blot of pSHIP1 and SHIP1 was performed as we previously described (*56*). Briefly, FO B cells were sorted and stimulated for 10 min following the same method described above. Whole anti-mouse IgM (Jackson ImmunoResearch) was used instead of anti-IgM F(ab′)2 to activate FcγRIIB. Stimulation was immediately ceased by adding ice-cold PBS. Cells were lysed in Cell Lysis buffer (BD Biosciences) supplemented with Halt Protease and Phosphatase Inhibitor Cocktail (Thermo Fisher Scientific) at 1×10^5 cells/3 μl. Capillary Western blot was performed with Jess (Protein Simple) according to the manufacturer's instruction. Obtained data were analyzed with Compass for SW software (Protein Simple). Area under the curve of band intensity histograms was used for protein amount quantification. Antibodies used are listed in table S1.

Proximity ligation assay

B cells were isolated from naïve mouse spleens with the EasySep Mouse Pan-B cell Isolation Kit (STEMCELL Technologies) and stimulated following the same method as BCR signal analyses described above. The proximity of the interested molecules was visualized using Duolink In Situ Detection reagents (Millipore Sigma) according to the manufacturer's instructions. Briefly, fixed cells were blocked for 50 min at 37°C and labeled with antibodies listed in table S1 for 30 min at room temperature in 96-well V-bottom plates. After a washing step, PLA probes were added in wells and incubated for an hour at 37°C. Cells were subsequently washed and incubated with ligase for 30 min at 37°C, followed by oligonucleotide amplification with DNA polymerase for 100 min at 37°C. Cell suspensions were applied to slide glasses using SHANDON Cytospin 4 (Thermo Fisher Scientific) and observed with a Zeiss Apoptome 3 microscope (Zeiss).

siRNA transfection

B cells were isolated from naïve mouse spleens with the EasySep Mouse Pan-B cell Isolation Kit (STEMCELL Technologies) and suspended in Opti-MEM I Reduced Serum Medium (Gibco). Each nAChR siRNA or control siRNA was cotransfected with BLOCK-iT Alexa Fluor Red Fluorescent Control (Thermo Fisher Scientific) to the cells using Lipofectamine RNAiMAX Reagent (Thermo Fisher Scientific), according to the manufacturer's instruction. Alexa Fluor 555–positive cells were sorted out by flow cytometry after 4 hours of incubation. Cells underwent further assays after additional 20 hours of culture in RPMI 1640 medium supplemented with 10% heat-inactivated FBS and 10 mM Hepes. siRNAs used are listed in table S1.

Statistical analysis

Statistical analysis was performed using Prism version 10 (GraphPad). P values < 0.05 were considered statistically significant. The values exceeding mean ± 3 SDs were considered outliers and removed. The statistical method used in each experiment is reported in the figure legends.

Supplementary Materials

This PDF file includes:

Figs. S1 to S6
Table S1

REFERENCES AND NOTES

1. B. Bonaz, V. Sinniger, D. Hoffmann, D. Clarençon, N. Mathieu, C. Dantzer, L. Vercueil, C. Picq, C. Trocmé, P. Faure, J.-L. Cracowski, S. Pellissier, Chronic vagus nerve stimulation in Crohn's disease: A 6-month follow-up pilot study. *Neurogastroenterol. Motil.* **28**, 948–953 (2016).
2. F. A. Koopman, S. S. Chavan, S. Miljko, S. Grazio, S. Sokolovic, P. R. Schuurman, A. D. Mehta, Y. A. Levine, M. Faltys, R. Zitnik, K. J. Tracey, P. P. Tak, Vagus nerve stimulation inhibits cytokine production and attenuates disease severity in Rheumatoid arthritis. *Proc. Natl. Acad. Sci. U.S.A.* **113**, 8284–8289 (2016).
3. H. Wang, M. Yu, M. Ochani, C. A. Amella, M. Tanovic, S. Susarla, J. H. Li, H. Wang, H. Yang, L. Ulloa, Y. Al-Abed, C. J. Czura, K. J. Tracey, Nicotinic acetylcholine receptor alpha7 subunit is an essential regulator of inflammation. *Nature* **421**, 384–388 (2003).
4. E. Meroni, N. Stakenborg, P. J. Gomez-Pinilla, M. Stakenborg, J. Aguilera-Lizarraga, M. Florens, M. Delfini, V. de Simone, G. De Hertogh, G. Goverse, G. Matteoli, G. E. Boeckxstaens, Vagus nerve stimulation promotes epithelial proliferation and controls colon monocyte infiltration During DSS-induced colitis. *Front. Med.* **8**, 694268 (2021).
5. T. Koren, A. Rolls, Immunoception: Defining brain-regulated immunity. *Neuron* **110**, 3425–3428 (2022).
6. V. A. Pavlov, S. S. Chavan, K. J. Tracey, Molecular and functional neuroscience in immunity. *Annu. Rev. Immunol.* **36**, 783–812 (2018).
7. H. Wang, H. Liao, M. Ochani, M. Justiniani, X. Lin, L. Yang, Y. Al-Abed, H. Wang, C. Metz, E. J. Miller, K. J. Tracey, L. Ulloa, Cholinergic agonists inhibit HMGB1 release and improve survival in experimental sepsis. *Nat. Med.* **10**, 1216–1221 (2004).
8. V. A. Pavlov, W. R. Parrish, M. Rosas-Ballina, M. Ochani, M. Puerta, K. Ochani, S. Chavan, Y. Al-Abed, K. J. Tracey, Brain acetylcholinesterase activity controls systemic cytokine levels through the cholinergic anti-inflammatory pathway. *Brain Behav. Immun.* **23**, 41–45 (2009).
9. Y.-J. Wu, L. Wang, C.-F. Ji, S.-F. Gu, Q. Yin, J. Zuo, The role of α7nAChR-mediated cholinergic anti-inflammatory pathway in immune cells. *Inflammation* **44**, 821–834 (2021).
10. M. Rosas-Ballina, P. S. Olofsson, M. Ochani, S. I. Valdés-Ferrer, Y. A. Levine, C. Reardon, M. W. Tusche, V. A. Pavlov, U. Andersson, S. Chavan, T. W. Mak, K. J. Tracey, Acetylcholine-synthesizing T cells relay neural signals in a vagus nerve circuit. *Science* **334**, 98–101 (2011).
11. T. Fujii, M. Mashimo, Y. Moriwaki, H. Misawa, S. Ono, K. Horiguchi, K. Kawashima, Expression and function of the cholinergic system in immune cells. *Front. Immunol.* **8**, 1085 (2017).
12. R. Fernandez, G. Nardocci, C. Navarro, E. P. Reyes, C. Acuña-Castillo, P. P. Cortes, Neural reflex regulation of systemic inflammation: Potential new targets for sepsis therapy. *Front. Physiol.* **5**, 489 (2014).
13. W. Kong, K. Kang, Y. Gao, H. Liu, X. Meng, Y. Cao, S. Yang, W. Liu, J. Zhang, K. Yu, M. Zhao, GTS-21 protected against lps-induced sepsis myocardial injury in mice through α7nAChR. *Inflammation* **41**, 1073–1083 (2018).
14. L. V. Borovikova, S. Ivanova, M. Zhang, H. Yang, G. I. Botchkina, L. R. Watkins, H. Wang, N. Abumrad, J. W. Eaton, K. J. Tracey, Vagus nerve stimulation attenuates the systemic inflammatory response to endotoxin. *Nature* **405**, 458–462 (2000).
15. M. Rana, Y. Fei-Bloom, M. Son, A. La Bella, M. Ochani, Y. A. Levine, P. Y. Chiu, P. Wang, S. S. Chavan, B. T. Volpe, B. Sherry, B. Diamond, Constitutive vagus nerve activation modulates immune suppression in sepsis survivors. *Front. Immunol.* **9**, 2032 (2018).
16. M. Rana, A. La Bella, R. Lederman, B. T. Volpe, B. Sherry, B. Diamond, Follicular dendritic cell dysfunction contributes to impaired antigen-specific humoral responses in sepsis-surviving mice. *J. Clin. Invest.* **131**, e146776 (2021).
17. K. Ekdahl, J. H. Braconier, C. Svanborg, Immunoglobulin deficiencies and impaired immune response to polysaccharide antigens in adult patients with recurrent community-acquired pneumonia. *Scand. J. Infect. Dis.* **29**, 401–407 (1997).

18. S. Martín, A. Pérez, C. Aldecoa, Sepsis and immunosenescence in the elderly patient: A review. *Front. Med.* **4**, 20 (2017).
19. C. Young, R. Brink, The unique biology of germinal center B cells. *Immunity* **54**, 1652–1664 (2021).
20. C. D. C. Allen, J. G. Cyster, Follicular dendritic cell networks of primary follicles and germinal centers: Phenotype and function. *Semin. Immunol.* **20**, 14–25 (2008).
21. C. G. Vinuesa, M. A. Linterman, D. Yu, I. C. M. MacLennan, Follicular helper T cells. *Annu. Rev. Immunol.* **34**, 335–368 (2016).
22. S. T. Chen, T. Y. Oliveira, A. Gazumyan, M. Cipolla, M. C. Nussenzweig, B cell receptor signaling in germinal centers prolongs survival and primes B cells for selection. *Immunity* **56**, 547–561.e7 (2023).
23. L. Koval, O. Lykhmus, M. Zhmak, A. Khruschov, V. Tsetlin, E. Magrini, A. Viola, A. Chernyavsky, J. Qian, S. Grando, S. Komisarenko, M. Skok, Differential involvement of α4β2, α7 and α9α10 nicotinic acetylcholine receptors in B lymphocyte activation in vitro. *Int. J. Biochem. Cell Biol.* **43**, 516–524 (2011).
24. X. Zhang, B. Lei, Y. Yuan, L. Zhang, L. Hu, S. Jin, B. Kang, X. Liao, W. Sun, F. Xu, Y. Zhong, J. Hu, H. Qi, Brain control of humoral immune responses amenable to behavioural modulation. *Nature* **581**, 204–208 (2020).
25. Z. You, B. Liu, H. Qi, Neuronal regulation of B-cell immunity: Anticipatory immune posturing? *Neuron* **110**, 3582–3596 (2022).
26. N. H. Bishopric, H. J. Cohen, R. J. Lefkowitz, Beta adrenergic receptors in lymphocyte subpopulations. *J. Allergy Clin. Immunol.* **65**, 29–33 (1980).
27. Y. X. Fujii, H. Fujigaya, Y. Moriwaki, H. Misawa, T. Kasahara, S. A. Grando, K. Kawashima, Enhanced serum antigen-specific IgG1 and proinflammatory cytokine production in nicotinic acetylcholine receptor α7 subunit gene knockout mice. *J. Neuroimmunol.* **189**, 69–74 (2007).
28. C. D. C. Allen, K. M. Ansel, C. Low, R. Lesley, H. Tamamura, N. Fujii, J. G. Cyster, Germinal center dark and light zone organization is mediated by CXCR4 and CXCR5. *Nat. Immunol.* **5**, 943–952 (2004).
29. C. Huang, H. Geng, I. Boss, L. Wang, A. Melnick, Cooperative transcriptional repression by BCL6 and BACH2 in germinal center B-cell differentiation. *Blood* **123**, 1012–1020 (2014).
30. A. L. Shaffer, X. Yu, Y. He, J. Boldrick, E. P. Chan, L. M. Staudt, BCL-6 represses genes that function in lymphocyte differentiation, inflammation, and cell cycle control. *Immunity* **13**, 199–212 (2000).
31. D. D. Chaplin, C. L. Zindl, Taking control of follicular dendritic cells. *Immunity* **24**, 13–15 (2006).
32. L. Duan, D. Liu, H. Chen, M. A. Mintz, M. Y. Chou, D. I. Kotov, Y. Xu, J. An, B. J. Laidlaw, J. G. Cyster, Follicular dendritic cells restrict interleukin-4 availability in germinal centers and foster memory B cell generation. *Immunity* **54**, 2256–2272.e6 (2021).
33. P. Avancena, T. Song, Y. Yao, H. Fehlner-Peach, B. Diamond, H. Gu, K. Rajewsky, Y. R. Zou, The magnitude of germinal center reactions is restricted by a fixed number of preexisting niches. *Proc. Natl. Acad. Sci. U.S.A.* **118**, e2100576118 (2021).
34. R. Endres, M. B. Alimzhanov, T. Plitz, A. Fütterer, M. H. Kosco-Vilbois, S. A. Nedospasov, K. Rajewsky, K. Pfeffer, Mature follicular dendritic cell networks depend on expression of lymphotoxin β receptor by radioresistant stromal cells and of lymphotoxin β and tumor necrosis factor by B cells. *J. Exp. Med.* **189**, 159–168 (1999).
35. P. Victoratos, J. Lagnel, S. Tzima, M. B. Alimzhanov, K. Rajewsky, M. Pasparakis, G. Kollias, FDC-specific functions of p55TNFR and IKK2 in the development of FDC networks and of antibody responses. *Immunity* **24**, 65–77 (2006).
36. M. E. El Shikh, R. El Sayed, A. K. Szakal, J. G. Tew, Follicular dendritic cell (FDC)-FcγRIIB engagementviaimmune complexes induces the activated FDC phenotype associated with secondary follicle development. *Eur. J. Immunol.* **36**, 2715–2724 (2006).
37. H. Yu, L. Lin, Z. Zhang, H. Zhang, H. Hu, Targeting NF-κB pathway for the therapy of diseases: Mechanism and clinical study. *Signal Transduct. Target. Ther.* **5**, 209 (2020).
38. M. R. Gold, M. P. Scheid, L. Santos, M. Dang-Lawson, R. A. Roth, L. Matsuuchi, V. Duronio, D. L. Krebs, The B cell antigen receptor activates the Akt (protein kinase B)/glycogen synthase kinase-3 signaling pathway via phosphatidylinositol 3-kinase. *J. Immunol.* **163**, 1894–1905 (1999).
39. T. Tiller, J. Kofer, C. Kreschel, C. E. Busse, S. Riebel, S. Wickert, F. Oden, M. M. M. Mertes, M. Ehlers, H. Wardemann, Development of self-reactive germinal center B cells and plasma cells in autoimmune FcγRIIB-deficient mice. *J. Exp. Med.* **207**, 2767–2778 (2010).
40. D. C. Otero, S. A. Omori, R. C. Rickert, CD19-dependent activation of Akt kinase in B-lymphocytes. *J. Biol. Chem.* **276**, 1474–1478 (2001).
41. S. Bolland, R. N. Pearse, T. Kurosaki, J. V. Ravetch, SHIP modulates immune receptor responses by regulating membrane association of Btk. *Immunity* **8**, 509–516 (1998).
42. C. Fabiani, V. N. Georgiev, D. A. Peñalva, L. Sigaut, L. Pietrasanta, J. Corradi, R. Dimova, S. S. Antollini, Membrane lipid organization and nicotinic acetylcholine receptor function: A two-way physiological relationship. *Arch. Biochem. Biophys.* **730**, 109413 (2022).
43. I. T. Mughrabi, J. Hickman, N. Jayaprakash, D. Thompson, U. Ahmed, E. S. Papadoyannis, Y. C. Chang, A. Abbas, T. Datta-Chaudhuri, E. H. Chang, T. P. Zanos, S. C. Lee, R. C. Froemke, K. J. Tracey, C. Welle, Y. Al-Abed, S. Zanos, Development and characterization of a chronic implant mouse model for vagus nerve stimulation. *eLife* **10**, e61270 (2021).
44. E. X. Albuquerque, E. F. R. Pereira, M. Alkondon, S. W. Rogers, Mammalian nicotinic acetylcholine receptors: From structure to function. *Physiol. Rev.* **89**, 73–120 (2009).
45. S. S. Chavan, V. A. Pavlov, K. J. Tracey, Mechanisms and therapeutic relevance of neuro-immune communication. *Immunity* **46**, 927–942 (2017).
46. V. M. Sanders, The beta2-adrenergic receptor on T and B lymphocytes: Do we understand it yet? *Brain Behav. Immun.* **26**, 195–200 (2012).
47. A. P. Kohm, A. Mozaffarian, V. M. Sanders, B cell receptor- and β 2 -Adrenergic receptor-induced regulation of B7-2 (CD86) expression in B cells. *J. Immunol.* **168**, 6314–6322 (2002).
48. R. Torres-Rosas, G. Yehia, G. Peña, P. Mishra, M. Del Rocio Thompson-Bonilla, M. A. Moreno-Eutimio, L. A. Arriaga-Pizano, A. Isibasi, L. Ulloa, Dopamine mediates vagal modulation of the immune system by electroacupuncture. *Nat. Med.* **20**, 291–295 (2014).
49. I. Papa, D. Saliba, M. Ponzoni, S. Bustamante, P. F. Canete, P. Gonzalez-Figueroa, H. A. McNamara, S. Valvo, M. Grimbaldeston, R. A. Sweet, H. Vohra, I. A. Cockburn, M. Meyer-Hermann, M. L. Dustin, C. Doglioni, C. G. Vinuesa, TFH-derived dopamine accelerates productive synapses in germinal centres. *Nature* **547**, 318–323 (2017).
50. E. J. Meredith, M. J. Holder, A. Rosén, A. D. Lee, M. J. S. Dyer, N. M. Barnes, J. Gordon, Dopamine targets cycling B cells independent of receptors/transporter for oxidative attack: Implications for non-Hodgkin's lymphoma. *Proc. Natl. Acad. Sci. U.S.A.* **103**, 13485–13490 (2006).
51. A. Nakai, Y. Hayano, F. Furuta, M. Noda, K. Suzuki, Control of lymphocyte egress from lymph nodes through β2-adrenergic receptors. *J. Exp. Med.* **211**, 2583–2598 (2014).
52. P. Sun, K. Zhou, S. Wang, P. Li, S. Chen, G. Lin, Y. Zhao, T. Wang, Involvement of MAPK / NF-κB signaling in the activation of the cholinergic anti-inflammatory pathway in experimental colitis by chronic vagus nerve stimulation. *PLOS ONE* **8**, e69424 (2013).
53. A. S. Caravaca, A. L. Gallina, L. Tarnawski, K. J. Tracey, V. A. Pavlov, Y. A. Levine, P. S. Olofsson, O. David, E. K. Ross, K. J. Otto, An effective method for acute vagus nerve stimulation in experimental inflammation. *Front. Neurosci.* **13**, 877 (2019).
54. H. C. Prescott, J. J. Osterholzer, K. M. Langa, D. C. Angus, T. J. Iwashyna, Late mortality after sepsis: Propensity matched cohort study. *BMJ* **353**, i2375 (2016).
55. L. E. Shupe, F. P. Miles, G. Jones, R. Yun, J. Mishler, I. Rembado, R. L. Murphy, S. I. Perlmutter, E. E. Fetz, Neurochip3: An Autonomous multichannel bidirectional brain-computer interface for closed-loop activity-dependent stimulation. *Front. Neurosci.* **15**, 718465 (2021).
56. A. N. Barlev, S. Malkiel, I. Kurata-Sato, A. L. Dorjée, J. Suurmond, B. Diamond, FcγRIIB regulates autoantibody responses by limiting marginal zone B cell activation. *J. Clin. Invest.* **132**, e157250 (2022).

Acknowledgments: We thank Flow Cytometry Core Facility and Microscopy Core Facility of the Feinstein Institutes for Medical Research for technical assistance. We also thank H. Khalili for assistance on performing single-cell RNA sequencing. **Funding:** This work is supported by Uehara Memorial Foundation Overseas Research Fellowship to I.K.-S. **Author contributions:** I.K.-S. and I.T.M. designed and conducted experiments, analyzed data, and wrote the manuscript. M.R. designed experiments. M.G. conducted experiments and analyzed data. Y.A.-A., S.Z., and B.S. conceptualized the study and designed experiments. B.D. conceptualized the study, designed experiments, interpreted data, and edited the manuscript. **Competing interests:** The authors declare that they have no competing interests. **Data and materials availability:** The single-cell RNA sequencing data are deposited in Gene Expression Omnibus https://ncbi.nlm.nih.gov/geo/ (accession number GSE246196). All other data needed to evaluate the conclusions in the paper are present in the paper and/or the Supplementary Materials.

Submitted 6 December 2023
Accepted 26 March 2024
Published 26 April 2024
10.1126/sciadv.adn3760